# Structure-property relationships in self-assembled metalorganic chemical vapor deposition–grown $CoFe_2O_4$–$PbTiO_3$ multiferroic nanocomposites using three-dimensional characterization

Mengchun Pan,[1,2,a)] Yuzi Liu,[2] Guoren Bai,[2] Seungbum Hong,[2] Vinayak P. Dravid,[1] and Amanda K. Petford-Long[1,3]
[1]*Department of Materials Science and Engineering, Northwestern University, Evanston, Illinois 60202, USA*
[2]*Materials Science Division, Argonne National Laboratory, Lemont, Illinois 60439, USA*
[3]*Center for Nanoscale Materials, Argonne National Laboratory, Lemont, Illinois 60439, USA*

(Received 14 April 2011; accepted 18 June 2011; published online 8 August 2011)

Multiferroic nanocomposites, consisting of branched, ferrimagnetic $CoFe_2O_4$ filaments and large protruding $PbTiO_3$ particles embedded in a piezoelectric $PbTiO_3$ matrix, have been fabricated by co-deposition using metalorganic chemical vapor deposition. Branched $CoFe_2O_4$ filaments reduce the $CoFe_2O_4$/$PbTiO_3$ interfacial strain and induce a perpendicular magnetic anisotropy. Three-dimensional characterizations reveal that in addition to the *c*-domain, grains with a second orientation in $PbTiO_3$ particles contribute to an additional four apparent variants of polarization. In contrast, the $PbTiO_3$ matrix exhibits only *c*-domain polarization with a smaller magnitude. The smaller piezoresponse results from the constraints imposed by the branched $CoFe_2O_4$ filaments. Three-dimensional microstructure and property analysis provide a comprehensive insight on the structure-property relationship of multiferroic nanocomposites grown by metalorganic chemical vapor deposition. © *2011 American Institute of Physics*. [doi:10.1063/1.3615888]

## I. INTRODUCTION

Artificial multiferroic heterostructures, consisting of ferroelectric and magnetic phases in close proximity, have aroused significant attention due to their novel physical properties, which originate from the interfacial coupling of structural, electric, and magnetic order parameters.[1–4] Approaches including synthesis of single-phase multiferroic materials, vertical heterostructures, and horizontal multilayers have demonstrated the possibility to achieve the coupling of ferroic properties.[1–4] The latter two approaches use the strain that arises at the interface between the heteroepitaxial ferroelectric and magnetic phases,[3,4] but vertical heterostructures are reported to induce higher coupling due to the capacity for a larger interfacial area between the two phases.[1,4,5] Zheng *et al.*[4] first deposited self-assembled $BaTiO_3$–$CoFe_2O_4$ multiferroic nanostructures using pulsed laser deposition (PLD). A change of magnetization at the ferroelectric transition temperature was demonstrated along with magnetic perpendicular anisotropy attributed to magnetoelasticity.[4] Subsequently, intensive experimental[6–8] and theoretical[8–10] work has focused on vertical nanostructures, consisting of heteroepitaxial spinel magnets embedded in perovskite ferroelectrics or vice versa, deposited on single crystal substrates.

The size and shape of features at nanoscale are critical to controlling their properties in devices,[11] and the ability to characterize such features in three dimensions (3 D) is of increasing importance in explaining functional properties. For example, magnetocrystalline anisotropy aligns the easy axis of magnetization along a certain direction with respect to the crystal structure,[12] and polarization domain structures usually correspond to a certain grain orientation or strain distribution in ferroelectric materials.[13] Electron tomography is a method that can reconstruct the 3 D shape of an object from a series of two-dimensional projections recorded at different view angles,[11,14] with a spatial resolution on the order of ~1 nm, a field of view of at least hundreds of nanometers, and the versatility to investigate microstructure and composition or diffraction information at the same time.[11,15–17] It is therefore an ideal technique to investigate both the morphology and chemistry of two-phase multiferroic nanocomposites on the nanoscale. Vector piezoresponse force microscopy (v-PFM) can be used to image local electromechanical responses, which are related to crystallographic orientation by piezoelectricity,[18] so v-PFM complements the microstructural information obtained by the transmission electron microscopy (TEM) techniques. In this paper we use scanning TEM (STEM) tomography and nanodiffraction to observe the 3 D microstructure and correlate it with the 3 D polarization domains imaged using v-PFM and with the magnetic anisotropy measured from magnetic hysteresis loops. The 3 D correlation of microstructure and functional properties offers understanding to the structure-property relationship of multiferroic heterostructures prepared by metalorganic chemical vapor deposition (MOCVD).

## II. EXPERIMENTAL DETAILS

$CoFe_2O_4$ (CFO)–$PbTiO_3$ (PTO) nanocomposite films (~280 nm thick) were co-deposited at 775 ± 5 °C on a single crystal (001) $SrTiO_3$ (STO) substrate using MOCVD. This substrate was chosen to obtain a *c*-axis oriented nanocomposite, given that the ferroelectricity of PTO is along the *c*-axis and

a)Author to whom correspondence should be addressed. Electronic mail: mengchunpan2008@u.northwestern.edu.

 

the magnetocrystalline anisotropy of CFO tends to align the magnetization along the ⟨100⟩ crystallographic directions.[12,13] During deposition, metal organic precursors, evaporated from solid phase cobalt tris(2,2,6,6-tetramethyl-3,5-heptanedionate) and iron(III) tris(2,2,6,6-tetramethyl-3,5-heptanedionate) and liquid phase tetraethyl lead, titanium (IV) t-butoixde, and $O_2$ gas simultaneously flowed to the deposition chamber in a home-built horizontal MOCVD system. An excess $O_2$ flow is to ensure an oxygen-rich environment for complete reactions. Since the heating plate elevated the temperature of the whole reactor into the window of deposition, cooling water was circulated on top of the chamber to avoid deposition on the wall and promote surface reaction of precursors on the substrate by creating a temperature gradient. After deposition, the nanocomposites were left to cool to room temperature in the reactor, under flowing $O_2$ gas.

The surface of the nanocomposites was imaged by an FEI Quanta 400 F scanning electron microscope (SEM) with 15 kV acceleration. Cross sectional (lamellar) and cylinder-shaped TEM samples were prepared by a Zeiss 1540XB focused ion beam–SEM cross beam system. A tungsten protective layer is essential to prevent damage from sample preparation using a focused ion beam and carbon is used as second protective layer and contrast medium between the tungsten and the specimen.[19,20] Elemental distribution, tomography, microstructure, and electron nanodiffraction were investigated in an FEI Tecnai F20ST S/TEM.

A Quantum Design MFMS-7 superconducting quantum interference device (SQUID) was used to collect magnetic hysteresis loops at 300 K. The applied field lies within 5° of the desired direction. The errors of measurement are about 10%, arising from the accuracy of SQUID measurements, the alignment of the field direction, and the estimation of the CFO volume. The volume of CFO filaments is estimated by the area percentage (~18%) of CFO phase in Fig. 1(a) multiplied by the thickness (~280 nm) measured in Fig. 1(b).

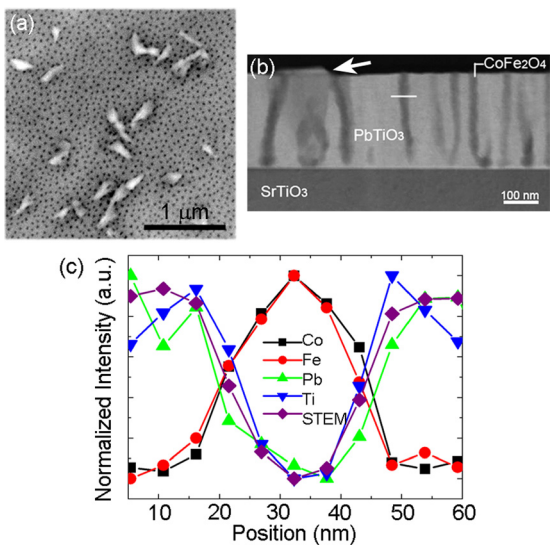


FIG. 1. (Color online) The morphology of the nanocomposites by (a) SEM and (b) cross-sectional STEM HAADF micrographs. The white line in (b) indicates the position where the EDS line scan was performed. The normalized elemental profile is shown in (c).

Piezoelectric domain configuration was probed by v-PFM using a lock-in amplifier (SR850, Stanford Research Systems) with a Pt-coated tip (PPP-EFM, Nanosensors). The ac modulation voltage applied to the tip was 2 $V_{rms}$ (root mean square) at 17 kHz. Since lateral-PFM detects the polarization components perpendicular to the cantilever axis, the x and y components of polarization were obtained by scanning the same area twice but physically rotating the sample 90° relative to the previous scan. The images shown in Fig. 5 were already rotated back to match the topography for clarity. Note the x and y are parallel to the crystallographic [100] direction of STO substrate. The piezoresponse magnitude was calibrated by using the average slope of the force-distance curves at different areas of the sample and the sensitivity of the lock-in amplifier.

## III. RESULTS AND DISCUSSION

Three different surface morphology features of CFO–PTO multiferroic nanocomposites on (001) STO fabricated by MOCVD can be distinguished in the SEM image seen in Fig. 1(a): ~20 nm small round grains, ~200 nm diameter large irregular particles, and the matrix. The area percentage of small grains is ~18% while the coverage of large particles is <3%. To investigate the internal morphology of the composite films and further determine composition, cross-sectional STEM high angle annual dark field (HAADF) imaging and energy dispersive X-ray spectroscopy (EDS) line scans were performed. The thickness of the composite film is determined as ~280 nm from the cross-sectional STEM HAADF image seen in Fig. 1(b); this value exceeds the typical critical thickness for the formation of misfit dislocations of individual CFO and PTO thin films on STO.[21,22] The dark filaments visible in Fig. 1(b) correspond to the ~20 nm small round surface features seen in the SEM image (Fig. 1(a)). The dark contrast indicates a lower average atomic number than the matrix. The details of the protruding parts of the filaments are not clearly resolved due to the low atomic number carbon cap layer. One large protruding grain showing intermediate HAADF contrast, with superimposed filaments, is marked by a white arrow in Fig. 1(b). To determine the composition of the different nanocomposite phases, an EDS line scan was performed across a single filament, at the position indicated by a white line in Fig. 1(b). The composition profile shown in Fig. 1(c) shows that the filaments contain more Co and Fe and the matrix contains more Pb and Ti, which suggest the filaments are CFO and the matrix is PTO. The average atomic number of CFO is lower than that of PTO, which explains why the filaments appear dark in the HAADF images. In addition, in Fig. 1(b), the two filaments on the right-hand side of the one analyzed using EDS appear to connect together, suggesting that the filaments are branched.

The 3 D morphology of the CFO filaments was analyzed using STEM electron tomography: Fig. 2 shows images recorded along two different viewing angles taken from lamellar (Figs. 2(a) and 2(b)) and cylinder-shaped (Figs. 2(c) and 2(d)) samples. The contrast in Fig. 2 is reversed using the CHIMERA[23] visualization software so that the bright contrast corresponds to the CFO filaments. Movies of rotating

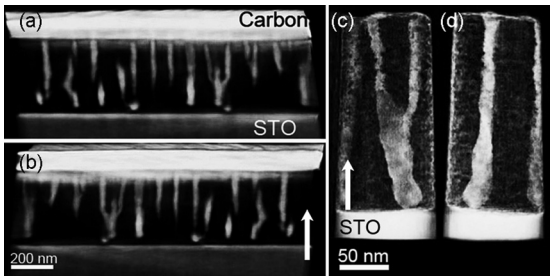


FIG. 2. Two representative viewing angles of STEM tomography data in a (a), (b) lamellar (enhanced online, Video 1) [URL: http://dx.doi.org/10.1063/1.3615888.1] and (c), (d) cylinder-shaped sample (enhanced online, Video 2) [URL: http://dx.doi.org/10.1063/1.3615888.2]. The white arrows indicate the growth direction.

filaments reconstructed from tilt series of STEM images can be found in the supplementary materials. The 3 D reconstruction of the filament microstructure is essential to establish connectivity of the filamentary grains. The long axis of the CFO filaments is not exactly parallel to the film normal, and none of the filaments seen in Figs. 2(a) and 2(b) are completely attached to the STO substrate surface. A more detailed 3 D structure of one double-branched filament is shown in Figs. 2(c) and 2(d), which confirms that the filament originates at a small distance from the STO surface. The region of the CFO filament closest to the STO surface (~28 nm thick) has an inverted cone shape, and the branching originates at least 30 nm away from the interface with the substrate. The filaments are either non-branched, double branched, or triple branched.

### A. Microstructure and growth mechanism of branched $CoFe_2O_4$ filaments embedded in the $PbTiO_3$ matrix

Electron nanodiffraction patterns recorded on a filament and on the matrix are shown in Fig. 3 together with a bright field TEM image. The diameter of the CFO filament (~20 nm) is smaller than the TEM sample thickness, and thus it overlaps with the PTO matrix in the TEM image except where it protrudes from the film surface. The electron nanodiffraction patterns in Figs. 3(b) and 3(c) are taken from the areas marked 1 and 2 in Fig. 3(a). The growth direction is indicated by a white arrow. The patterns confirm the matrix as PTO and the filaments as CFO, consistent with the EDS elemental profile in Fig. 1(c). Both the CFO filaments and the PTO matrix have the [001] crystallographic direction parallel to the substrate normal. The orientation relationship between the CFO filaments, PTO matrix, and STO substrate

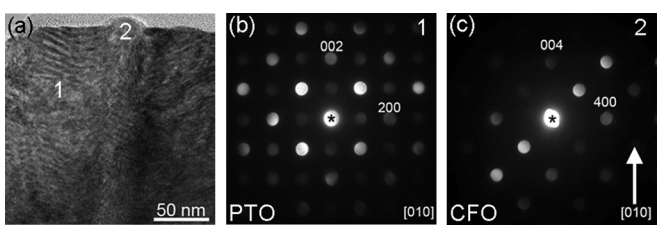


FIG. 3. The electron nanodiffraction of areas 1 (PTO) and 2 (CFO) marked in (a) are shown in (b) and (c), respectively. The white arrow indicates the growth direction.

is: $PTO_{(001)[010]}//CFO_{(001)[010]}//STO_{(001)[010]}$. The *c*-axis oriented PTO matrix is expected since the in-plane lattice parameter of PTO is closer to the lattice parameter of cubic phase STO and the stress at the interface will thus be smaller for *c*-axis oriented PTO.[24,25]

The geometry of the nanocomposites, namely CFO filaments embedded in a PTO matrix, can be explained by considering the growth mode. At the onset of deposition, constraint from the substrate leads to competition between the surface and interface energies.[9] The surface energy of the (001) PTO planes is lower than that of the (001) CFO planes,[26–28] leading to a higher sticking coefficient and thus higher nucleation rate for PTO on the STO substrate. Furthermore, the MOCVD growth rate for PTO is higher than that for CFO, based on the thickness of single layer CFO and PTO thin films grown with the same total pressure and growth temperature for the same amount of time.[29,30] This means that during co-deposition, the partial pressure of Pb and Ti precursors in the gas phase are higher than those of Co and Fe. A combination of the lower surface energy of PTO on STO, and more Pb and Ti precursors in the gas phase, leads to the PTO phase wetting the STO surface at the onset of deposition, and results in the formation of CFO filaments in a PTO matrix with an area fraction of ~18%. In a phase field simulation model, in which clusters are considered as elastic domains during growth, the importance of elastic energy developed at the substrate/nanostructure interface is emphasized rather than a film/substrate orientation dominated by interfacial energies.[8,10] For MOCVD growth, both film/substrate orientation and the high PTO volume fraction result in PTO being the matrix phase. The inverted cone morphology (~28 nm thick) observed at the bottom of the CFO filaments is similar to the CFO phase observed in a 30 nm thick CFO–PTO nanostructure deposited on (001) STO using PLD.[7] The formation of the cone shape is attributed to the fact that the lowest interphase energy in the growing film is between the {111} planes of CFO and PTO.[7]

The cross-sectional size of the CFO filaments grown by MOCVD (20 nm diameter in a ~280 nm thick film) is smaller than those grown by PLD (long edge of 50 nm in a ~230 nm thick film) and smaller than predicted by the phase field simulation model (long edge of 100 nm when equilibrium is achieved).[7] The cross-sectional shapes of MOCVD-grown filaments are nearly round instead of rectangular with edges along the ⟨110⟩ directions as observed for PLD growth and in models. The different morphology may result from a diffusion process during growth and interphase strain between the CFO and PTO resulting from the high PTO volume fraction. Neither factor is considered in the phase field model.[8,10] Since diffusion of precursors is essential for occurrence of chemical reactions during MOCVD,[31] it is believed that this diffusion is the controlling process rather than interphase strain, which would be expected to restrict the CFO phase to develop into an equilibrium rectangular shape with preferred edge directions.[10]

The difference in interface energies (both between the CFO and PTO, and at the substrate/film interface), and in growth rates between PTO and CFO, are responsible for the distribution of the two phases and their morphology close to the substrate, but not for the formation of CFO branches.

The filament branches originate at least 30 nm away from the interface, above the critical thickness of coherent-strained CFO thin films on STO and close to the critical thickness of coherent-strained PTO thin films on STO.[21,22] During deposition using MOCVD, the chemical reactions occur at energy favorable sites, usually close to previous nucleation sites of the same phase but not necessarily on top of them.[31] This could result in CFO filaments growing at a small angle with respect to substrate normal, and then being constrained by the surrounding, growing PTO. At the same time, the PTO phase starts to relax, offering strain relaxation sites that allow the CFO filaments to branch. Furthermore, branching of the CFO filaments allows for further strain relaxation between CFO and PTO phases, similar to the {111} nanofacets that can develop during PLD growth.[7]

### B. Microstructure and growth mechanism of large protruding $PbTiO_3$ particles

The microstructure of the large protruding $PbTiO_3$ particles was also investigated by electron nanodiffraction. A TEM bright field image and the corresponding electron nanodiffraction patterns from two areas are shown in Figs. 4(a), 4(b), and 4(c) with the growth direction indicated by black arrows. The electron nanodiffraction of area 3 corresponds to PTO with the [001] direction parallel to film normal: the same orientation as the PTO matrix. However, the diffraction pattern from area 4 contains two sets of lattice spots: one subset is consistent with the [010] zone axis of CFO and the other with the [212] zone axis of PTO. The energy filtered TEM image (not shown) from the same area shows an extended region with concentrated Co signal in area 4, and the CFO is thus believed to be part of a filament. However, the growth direction of PTO in area 4 is along $[2\bar{2}\bar{1}]$, which is different from that of PTO matrix though still parallel that of CFO [004]. Also, the nanodiffraction patterns

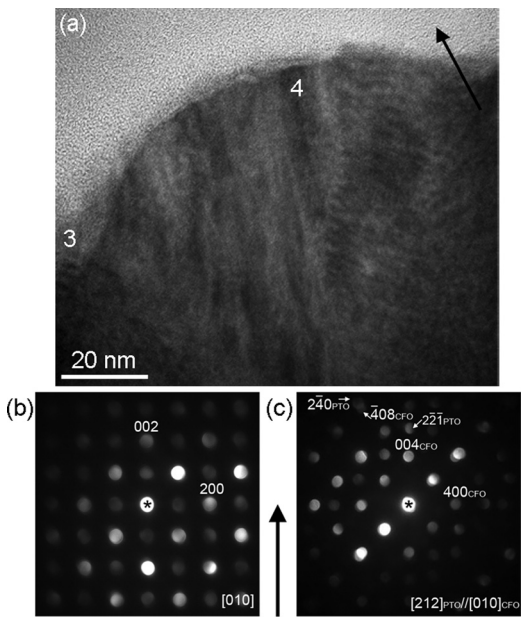


FIG. 4. The electron nanodiffraction patterns of areas 3 and 4 marked in (a) are shown in (b) and (c). The black arrows indicate the growth direction.

in Fig. 4(c) shows PTO $(2\bar{4}0)$ is parallel to CFO$(\bar{4}08)$. Since the epitaxial relationship of CFO and STO is previously established in Fig. 3 as $CFO_{(001)[010]}//STO_{(001)[010]}$, the epitaxial relationship in this area is thus: $PTO_{(1\bar{2}0)[212]}//CFO_{(\bar{1}02)[010]}//STO_{(\bar{1}02)[010]}$

The formation of the large protruding particles is believed to be the result of gas phase reaction at high temperature during MOCVD deposition. Although the MOCVD chamber is water-cooled, the temperature inside the chamber is still sufficient to sustain gas phase reactions due to the broad deposition temperature window for both CFO and PTO.[29,30] Grains produced in the gas phase reactions are not constrained in terms of orientation. However, when they land on the developing nanocomposite during deposition, diffusion helps to incorporate them into the filament-matrix geometry and orientation to minimize interface energies. Toward the end of the deposition process, the diffusion of precursors and gas phase reactions products becomes more limited and, thus, gas phase reaction products can be incorporated into the growing film at different orientations, as is seen for the large particles with growth direction along $[2\bar{2}1]$.

### C. Functional (piezoelectric and magnetic) properties of the multiferroic nanocomposites

To investigate the multiferroic properties of the self-assembled CFO–PTO nanocomposites, their piezoelectric and magnetic properties are studied. v-PFM was used to reconstruct the 3 D polarization domains of the nanocomposites.[18,32,33] Figure 5(a) shows the topography of the area of interest and Fig. 5(b) shows the relationship between crystallographic orientation of the STO substrate and the direction of the measured components of polarization. As expected, the CFO filaments do not exhibit a piezoresponse. For the PTO matrix, the phase contrast is uniformly bright in vertical PFM (Fig. 5(d)) with no signal visible in the lateral PFM images (Figs. 5(f) and 5(g)), indicating that the polarization in the PTO matrix points into the plane of the surface, denoted as the −z direction. This is shown qualitatively in Fig. 5(i). The single domain structure of the PTO matrix results from its *c*-axis oriented grain structure. Note that the small amplitude around the CFO filaments in the lateral PFM images (Figs. 5(e) and 5(g)) is a scanning artifact due to the sudden height change between the CFO filaments and the PTO matrix since those contrasts are always perpendicular to the scanning direction and the phases are merely noise in Figs. 5(f) and 5(h). The large PTO particles, however, exhibit a significantly higher piezoresponse, with x, y, and z components of polarization. The directions of the z components of the large PTO particles are identical to those of the matrix, confirmed by the overall bright contrast in Fig. 5(d). Figure 5(j) illustrates the six possible variants of polarization direction in the large PTO particles, with the viewing direction along PTO $[2\bar{2}1]$, i.e., the light gray box outlines a projection of the PTO unit cell along the $[2\bar{2}1]$ direction. A, B, and C are the projections of possible orientations of the [001] directions (along which the polarization lies). Possibly due to the small angle between A and B, only four variants

(C, A+B) are more apparent when probed using v-PFM. Two examples of the polarization distribution in particles 5 and 6 are given in Fig. 5(j). There are three distinct domains in particles 5 and 6. The middle domain only presents an out-of-plane polarization while the outer two domains possess in-plane polarization components. The in-plane polarization components are along the long axis of the PTO particles and point toward opposite directions in the two

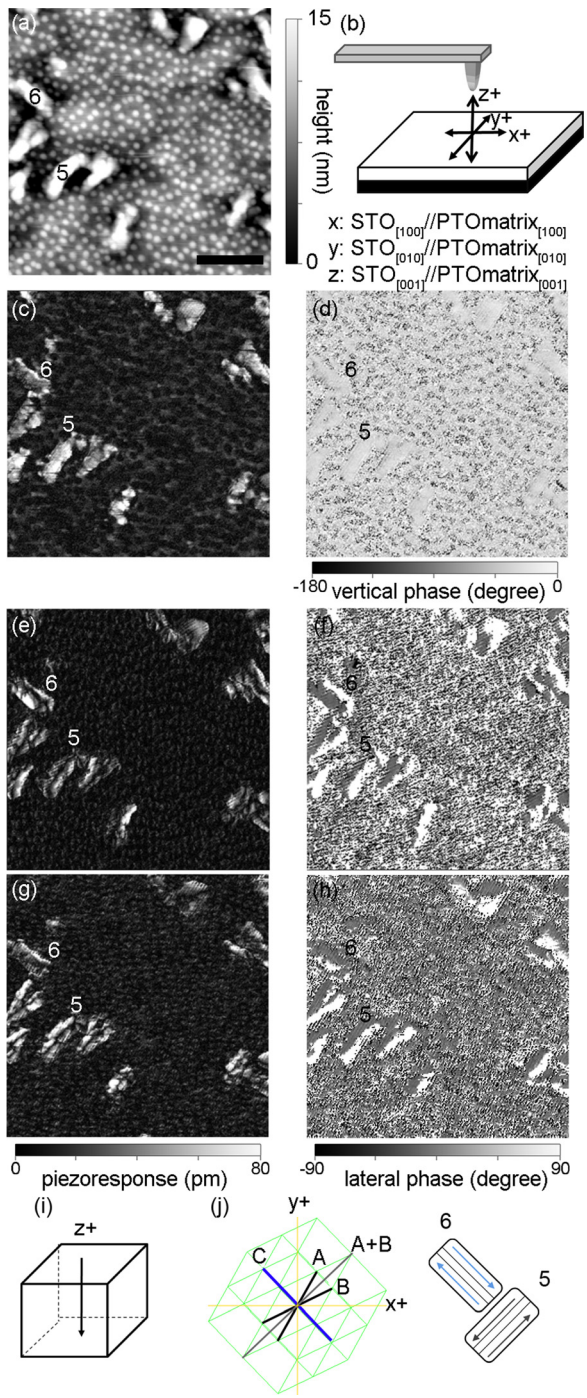


FIG. 5. (Color online) (a) Surface topography where vector PFM is performed, (b) illustration of coordinates in vector PFM, (c) vertical PFM amplitude and (d) phase, (e) lateral PFM along the x direction amplitude and (f) phase, (g) lateral PFM along the y direction amplitude and (h) phase, (i) polarization direction in PTO matrix and (j) variants of polarization directions in PTO particles with polarization map two representative PTO particles (particles 5 and 6). The scale bar is 500 nm.

domains in the same particle to minimize the electrostatic energies. In Fig. 5(c), the appearance of a dark circle of ~20 nm diameter in particle 5 indicates a region with no out-of-plane piezoresponse. This suggests that a CFO filament is buried beneath the large PTO particle. The microstructure of such a case is shown in Fig. 4. The multidomain structures are attributed to the fact that the large protruding PTO particles are composed of two grain orientations, [001] and $[2\bar{2}1]$, parallel to the substrate normal. [001] grains as the middle domain in the particle only have the *c*-domain whereas in-plane piezoresponses exist in the $[2\bar{2}1]$ grains. In an electron diffraction pattern, the structural variants with *c*-axis along the directions A, B, and C cannot be distinguished, but from the 3 D polarization maps of the domains, the four apparent variants *can* be distinguished.

The piezoelectric coefficient $d_{zz}$ can be roughly estimated as $d_{zz}$ = average vertical piezoresponse/applied bias, in spite of inhomogeneous strain and electric field under the PFM tip.[34] Using this method, Tan *et al.*[34] obtained $d_{zz\ (PTO\ matrix,\ non\text{-}branched)} \approx 11$ pm/V in their non-branched CFO filaments in PTO matrix (1/3PTO–2/3CFO) nanocomposites. In our nanocomposites, the $d_{zz}$ of PTO matrix and PTO particles are calculated to be $d_{zz\ (PTO\ matrix,\ branched)} \approx$ 4.35 pm/V and $d_{zz(PTO\ particles)} \approx 17$ pm/V respectively. Estimated value of $d_{zz}$ represents the intrinsic piezoresponse of the PTO phase in the nanocomposites under the mechanical and depolarizing-field constraints of the CFO phase.[34] The piezoresponse from the PTO matrix is smaller than from the PTO large particles as seen in Fig. 5(b) (smaller $d_{zz\ (PTO\ matrix,\ branched)}$) because the confinement from the high density of CFO filaments hinders the volume change of the PTO matrix under an applied bias. The higher piezoresponse of the large PTO particles is believed to arise from the fact that most of the PTO particles protrude from the nanocomposite surface, so they are less constrained by the CFO filaments. Furthermore, the value of $d_{zz\ (PTO\ matrix,\ non\text{-}branched)}$ (Ref. 34) is larger than our $d_{zz\ (PTO\ matrix,\ branched)}$, inferring that branched CFO filaments may impose larger constraints on the PTO matrix compared with the non-branched CFO filaments. The higher surface-to-volume ratio of branched CFO filaments is likely to contribute to the higher confinement strength of the PTO matrix.

To examine the magnetic properties of the CFO–PTO nanocomposites, magnetic hysteresis (M-H) loops were

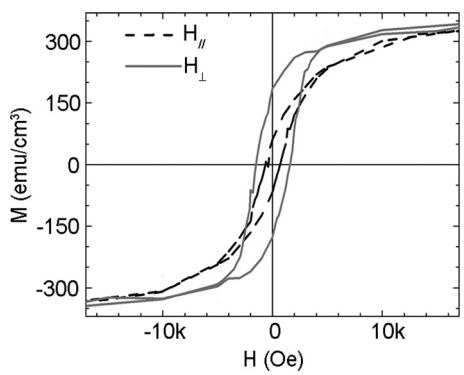


FIG. 6. Parallel ($H_{//}$) and perpendicular ($H_{\perp}$) magnetic hysteresis loops of CFO-PTO nanocomposite film.

recorded at 300 K using a SQUID. Figure 6 shows M-H loops with the field applied parallel to the in-plane [100] direction and the out-of-plane [001] direction (i.e., along the long axis of CFO filaments). Since the CFO filaments are branched, the CFO volume is slightly over-estimated by considering the area coverage fraction seen in Fig. 1. $M_s$ measured from both the [100] and [001] loops is about 340 emu/cm$^3$, smaller than the bulk value 400 emu/cm$^3$ but similar to the value for CFO epitaxial thin films on STO.[12,30] $M_r$ is 63 emu/cm$^3$ and 180 emu/cm$^3$ for [100] and [001] loops, respectively, and $H_c$ is 636 Oe for the [100] loop and 1626 Oe for the [001] loop. These data suggest that the easy axis is parallel to the long axis of the CFO filaments as opposed to the in-plane [100] direction favored in blanket CFO thin films. The anisotropy between the in-plane and out-of-plane directions is more significant than reported for blanket CFO thin films with a rough surface[30] but less significant than reported for $CoFe_2O_4$–$BaTiO_3$ (BTO) self-assembled nanostructures.[4] Zheng *et al*[4] argued that in CFO–BTO nanostructures, the out-of-plane compressive strain of the CFO phase resulting from the cubic-tetragonal structural distortion in the BTO matrix dominates the shape anisotropy and aligns the easy axis parallel to the axis of the CFO filaments. However, in our CFO–PTO nanocomposite thin films, the inter-phase strain is greatly relieved via the formation of branches in the CFO filaments, and a reduced anisotropy between the two directions is observed. Therefore, the shape anisotropy arising from the high aspect ratio of the CFO filaments (20 nm in diameter versus 280 nm in length) dominates and aligns the easy axis of magnetization along the out-of-plane [001] direction.

## IV. CONCLUSIONS

We applied a combination of 3 D characterization techniques to study the microstructure and functional properties of MOCVD-grown CFO–PTO nanocomposite films. The 3 D analysis offers insights to relate the growth mechanism, and magnetic and piezoresponse behavior of multiferroic nanocomposites. The nanocomposite films consist of CFO filaments embedded in PTO: this microstructure arises because of competition between the interfacial energies of PTO/STO and CFO/STO, and because of the difference in growth rates of CFO and PTO. The high aspect ratio of the CFO filaments allows the shape anisotropy to dominate the perpendicular magnetic anisotropy. The piezoelectric behavior is dominated by the large PTO particles formed by the gas phase reaction during MOCVD. The particles each contain two different grain orientations: [001] and [$2\overline{2}1$] parallel to the film normal. The existence of the second orientation leads to an additional four variants of polarization direction besides the common *c*-domains in the PTO matrix. The effective $d_{zz}$ of the large PTO particles is greater than that of the matrix due to the constraints on the matrix imposed by the non-piezoelectric CFO filaments.

## ACKNOWLEDGMENTS

The submitted manuscript has been created by UChicago Argonne, LLC, Operator of Argonne National Laboratory ("Argonne"). Argonne, a U.S. Department of Energy (DOE) Office of Science laboratory, is operated under Contract No. DE-AC02-06CH11357. Use of the Electron Microscopy Center of Argonne National Laboratory is gratefully acknowledged. The authors would like to thank Bernd Kabius and Daniel Schreiber for their insights to STEM and tomography sample preparation. John Pearson and Axel Hoffman are acknowledged for their assistance in SQUID measurements. The 3 D images of electron tomography were produced using the UCSF CHIMERA package from the Resource for Biocomputing, Visualization, and Informatics at the University of California, San Francisco (supported by NIH P41 RR-01081). See supplementary material at E-JAPIAU-110-007115 for the movies of tomography reconstructions of lamellar and cylinder-shaped samples.

[1]R. Ramesh and N. A. Spaldin, Nature Mater. **6**, 21 (2007).
[2]J. Wang, J. B. Neaton, H. Zheng, V. Nagarajan, S. B. Ogale, B. Liu, D. Viehland, V. Vaithyanathan, D. G. Schlom, U. V. Waghmare, N. A. Spaldin, K. M. Rabe, M. Wuttig, and R. Ramesh, Science **299**, 1719 (2003).
[3]G. Srinivasan, E. T. Rasmussen, J. Gallegos, R. Srinivasan, Y. I. Bokhan and V. M. Laletin, Physical Review B **6421**, 214408 (2001).
[4]H. Zheng, J. Wang, S. E. Lofland, Z. Ma, L. Mohaddes-Ardabili, T. Zhao, L. Salamanca-Riba, S. R. Shinde, S. B. Ogale, F. Bai, D. Viehland, Y. Jia, D. G. Schlom, M. Wuttig, A. Roytburd, and R. Ramesh, Science **303**, 661 (2004).
[5]M. Liu, X. Li, J. Lou, S. J. Zheng, K. Du, and N. X. Sun, J. Appl. Phys. **102**, 083911 (2007).
[6]J. X. Zhang, J. Y. Dai, W. Lu, H. L. W. Chan, B. Wu, and D. X. Li, J. Phys. D: Appl. Phys. **41**, 235405 (2008).
[7]Z. P. Tan, J. Slutsker, and A. L. Roytburd, J. Appl. Phys. **105**, 061615 (2009).
[8]I. Levin, J. H. Li, J. Slutsker, and A. L. Roytburd, Adv. Mater. **18**, 2044 (2006).
[9]H. Zheng, Q. Zhan, F. Zavaliche, M. Sherburne, F. Straub, M. P. Cruz, L. Q. Chen, U. Dahmen, and R. Ramesh, Nano Lett. **6**, 1401 (2006).
[10]J. Slutsker, I. Levin, J. H. Li, A. Artemev, and A. L. Roytburd, Phys. Rev. B **73**, 184127 (2006).
[11]P. A. Midgley and M. Weyland, Ultramicroscopy **96**, 413 (2003).
[12]H. Shenker, Phys. Rev. **107**, 1246 (1957).
[13]D. G. Schlom, L. Q. Chen, C. B. Eom, K. M. Rabe, S. K. Streiffer, and J. M. Triscone, Annu. Rev. Mater. Res. **37**, 589 (2007).
[14]F. Joachim, *Electron Tomography: Methods for Three-Dimensional Visualization of Structures in the Cell* (Springer, Berlin, 2006).
[15]I. Arslan, T. J. V. Yates, N. D. Browning, and P. A. Midgley, Science **309**, 2195 (2005).
[16]H. S. Kim, Y. Myung, Y. J. Cho, D. M. Jang, C. S. Jung, J. Park, and J. P. Ahn, Nano Lett. **10**, 1682 (2010).
[17]Y. Liu, A. Petford-Long, D. Schreiber, Y. S. Choi, D. Djayaprawira, and D. Seidman, Microsc. Microanal. **15** (Supplement S2), 1248 (2009).
[18]S. V. Kalinin, B. J. Rodriguez, S. Jesse, J. Shin, A. P. Baddorf, P. Gupta, H. Jain, D. B. Williams, and A. Gruverman, Microsc. Microanal. **12**, 206 (2006).
[19]T. Yaguchi, T. Kamino, T. Ishitani, and R. Urao, Microsc. Microanal. **5**, 365 (1999).
[20]N. I. Kato, Y. Kohno, and H. Saka, J. Vac. Sci. Technol. A **17**, 1201 (1999).
[21]M. Ohring, *Materials science of thin films* (Academic Press, New York, 2002).
[22]J. S. Speck and W. Pompe, J. Appl. Phys. **76**, 466 (1994).
[23]E. F. Pettersen, T. D. Goddard, C. C. Huang, G. S. Couch, D. M. Greenblatt, E. C. Meng, and T. E. Ferrin, J. Comput. Chem. **25**, 1605 (2004).
[24]B. S. Kwak, A. Erbil, J. D. Budai, M. F. Chisholm, L. A. Boatner, and B. J. Wilkens, Phys. Rev. B **49**, 14865 (1994).
[25]Q. Y. Qiu, V. Nagarajan, and S. P. Alpay, Phys. Rev. B **78**, 064117 (2008).
[26]J. Padilla and D. Vanderbilt, Surf. Sci. **418**, 64 (1998).

[27]B. Meyer, J. Padilla, and D. Vanderbilt, Faraday Discuss. **114**, 395 (1999).
[28]R. K. Mishra and G. Thomas, J. Appl. Phys. **48**, 4576 (1977).
[29]C. M. Foster, G. R. Bai, R. Csencsits, J. Vetrone, R. Jammy, L. A. Wills, E. Carr, and J. Amano, J. Appl. Phys. **81**, 2349 (1997).
[30]M. Pan, G. Bai, Y. Liu, S. Hong, V. P. Dravid, and A. K. Petford-Long, J. Appl. Phys. **107**, 043908 (2010).
[31]A. W. Vere, *Crystal Growth: Principles and Progress* (Plenum Press, New York, 1987).
[32]S. Hong, J. A. Klug, M. Park, A. Imre, M. J. Bedzyk, K. No, A. Petford-Long, and O. Auciello, J. Appl. Phys. **105**, 061619 (2009).
[33]R. Nath, S. Hong, J. A. Klug, A. Imre, M. J. Bedzyk, R. S. Katiyar and O. Auciello, Appl. Phys. Lett. **96**, 163101 (2010).
[34]Z. P. Tan, A. L. Roytburd, I. Levin, K. Seal, B. J. Rodriguez, S. Jesse, S. Kalinin, and A. Baddorf, Appl. Phys. Lett. **93**, 074101 (2008).